Near-Surface Full-Waveform Inversion Reveals Bedrock Controls on Critical Zone Architecture

B.J. Eppinger[1], W.S. Holbrook[1], Z. Liu[2], B.A. Flinchum[3], J. Tromp[4,5]

[1]Department of Geosciences, Virginia Polytechnic Institute and State University, Blacksburg, VA, USA

[2]Ocean University of China, Qingdao, China; Previously, Department of Geosciences, Princeton University, Princeton, NJ, USA

[3]Clemson University, Environmental Engineering and Earth Sciences, Clemson, SC, USA

[4]Department of Geosciences, Princeton University, Princeton, NJ, USA

[5]Program in Applied & Computational Mathematics, Princeton University, Princeton, NJ 08544-1000, USA

Key Points:

- We perform full-waveform inversion on shallow seismic refraction data to study critical zone architecture in the Laramie Range, Wyoming.
- Borehole data confirm that the full-waveform inversion result is more accurate than conventional traveltime tomography.
- The full-waveform inversion model reveals critical zone heterogeneity likely caused by lateral changes in bedrock properties.

Corresponding author: Benjamin Eppinger, `beppinger@vt.edu`

Abstract

For decades, seismic imaging methods have been used to study the critical zone, Earth's thin, life-supporting skin. The vast majority of critical zone seismic studies use traveltime tomography, which poorly resolves heterogeneity at many scales relevant to near-surface processes, therefore, limiting progress in critical zone science. Full-waveform inversion can overcome this limitation by leveraging more of the seismic waveform and enhancing the resolution of geophysical imaging. In this study, we apply full-waveform inversion to elucidate previously undetected heterogeneity in the critical zone at a well-studied catchment in the Laramie Range, Wyoming. In contrast to traveltime tomograms from the same data set, our results show variations in depth to bedrock ranging from 5 to 60 meters over lateral scales of just tens of meters and image steep low-velocity anomalies suggesting hydrologic pathways into the deep critical zone. Our results also show that areas with thick fractured bedrock layers correspond to zones of slightly lower velocities in the deep bedrock, while zones of high bedrock velocity correspond to sharp vertical transitions from bedrock to saprolite. By corroborating these findings with borehole imagery, we hypothesize that lateral changes in bedrock fracture density majorly impact critical zone architecture. Borehole data also show that our full-waveform inversion results agree significantly better with velocity logs than previously published traveltime tomography models. Full-waveform inversion thus appears unprecedently capable of imaging the spatially complex porosity structure crucial to critical zone hydrology and processes.

Plain Language Summary

Weathering processes within Earth's shallow subsurface break down rock into porous, mineral-rich materials from which biota can access water and garner nutrients. Therefore, knowledge about weathering helps scientists better understand how Earth supports terrestrial life. An effective way of studying weathering is seismic imaging, where by listening at Earth's surface to how mechanical waves propagate, we can make pictures of what is below and observe weathering in action. The seismic imaging method usually used to study weathering is first arrival traveltime tomography which produces blurry pictures of the subsurface. We applied an advanced seismic imaging technique called full-waveform inversion, which produces higher-resolution images. Our full-waveform inversion pictures imply that changes in bedrock fracture density over relatively small lateral

distances have a significant effect on how weathering processes operate. When the fracture density in the bedrock is low, there is a sharp transition from highly weathered materials to unaltered bedrock below. When the fracture density is high, the transition is more diffuse, and there exists a thick layer of weathered bedrock. Additionally, we ground-truth these interpretations with in-situ observations made in boreholes. Hence, full-waveform inversion appears capable of revealing new insights into subsurface structure and weathering processes.

1 Introduction

Nearly all terrestrial life resides in the critical zone (CZ), the volume spanning the roof of vegetation down to the top of bedrock. Soil, saprolite, and weathered bedrock within the CZ support terrestrial life by supplying water and nutrients to vegetation (e.g., Brantley et al., 2007; Hahm et al., 2013; McCormick et al., 2021). Weathering processes are fundamental to CZ structure and function by creating porosity and permeability for groundwater and by releasing nutrients from bedrock for biological uptake (e.g., Dawson et al. 2020; Hahm et al. 2019; Klos et al., 2018; McCormick et al. 2021; Meunier et al., 2007; Navarre-Sitchler et al., 2015; Riebe et al., 2016). In eroding landscapes, weathering processes sculpt a CZ architecture that generally consists of, from top to bottom, soil, saprolite, weathered/fractured bedrock, and finally intact/unweathered bedrock. While this layered framework is a useful starting point, CZ structure varies strongly, both within and between sites (e.g., Basilevskaya et al., 2013; St. Clair et al., 2015). Understanding the magnitude and scales of CZ heterogeneity requires improved knowledge of subsurface structure.

Because direct observations of the subsurface portion of the CZ are difficult, requiring trenches, soil pits, or boreholes, geophysical imaging is often used to study the shallow subsurface (e.g., Parsekian et al., 2015). Seismic imaging has the advantage of being primarily sensitive to porosity (e.g., Callahan et al., 2020; Flinchum et al., 2018; Hayes et al., 2019; Holbrook et al., 2014), which determines subsurface water storage capacity and reflects chemical and physical weathering in eroding landscapes. In the near-surface, the seismic methods most commonly used are first-arrival traveltime tomography (FATT) and multichannel analysis of surface waves (MASW). These methods have been reliably applied in engineering and research contexts for decades (e.g., Pasquet et al., 2016; Xia et al., 1999). In particular, FATT has been used extensively to study variations in CZ

architecture at scales of tens of meters (e.g., Befus et al., 2011; Holbrook et al., 2014; Callahan et al., 2022; Huang et al., 2021; St. Clair et al., 2015).

Despite the utility of FATT and MASW methods, CZ outcrops and boreholes typically show much more compositional and structural heterogeneity than is captured in typical seismic images. For example, borehole logs and recovered core often show small-scale weathering zones, corestones, root systems, compositional variations, and fractures that are not visible in smooth FATT velocity models at the same location (e.g., Flinchum et al., 2022; Holbrook et al., 2019; Moravec et al., 2020). This implies that typical geophysical views of the subsurface are blurry, eliding details about CZ structure, and by extension, hydrological and weathering processes. Improved resolution would enable detection of smaller-scale heterogeneities relevant to the hydrology, biology, and geochemistry of the critical zone. Full-waveform inversion offers a means to accomplish this.

Full-waveform inversion (FWI) is a seismic imaging technique that can improve the flexibility, fidelity, and resolution of seismic inversion by modeling the phase and/or amplitude of seismic arrivals, rather than just the arrival time. FWI is more flexible than other methods because it can be applied to any part of the waveform (e.g., body waves, surface waves, reflections, etc.). Fidelity is improved because FWI methods apply more accurate representations of the physics governing wave propagation than, say, ray-based approximations to the wave equation used in FATT or the 1D assumptions common in MASW. Resolution is enhanced because FWI leverages more of the seismic waveform than other methods of seismic inversion (e.g., Fichtner, 2010; Schuster, 2017). As a result, FWI has been widely applied in global and exploration seismology (Choi and Alkhalifah, 2012; Lei et al., 2020; Mao et al., 2016; Pratt, 1999; Virieux and Operto, 2009). To date, however, FWI has only been applied to the near surface in a handful of studies (e.g, Kohn et al., 2019; Liu et al., 2022; Sheng et al., 2006; Wang et al., 2019a, b, c).

Application of FWI to near-surface seismic data faces numerous challenges. First is the considerable computational expense and technical overhead associated with FWI as compared to FATT and MASW. Another hurdle in applying FWI is the need for domain-specific inversion strategies. For example, workflows used for inverting global seismology data, land seismic data, and marine reflection data all vary greatly (eg., Borisov et al., 2020; Lei et al., 2020; Mao et al., 2016). FWI in the near surface is also challenging because of the strong velocity contrasts and heterogeneity in elastic properties due to

the rapid compaction of regolith (e.g, Kohn et al., 2019; Liu et al., 2022; Sheng et al., 2006). Given the limited application of FWI to study the CZ, best practices remain ambiguous. A major goal of this paper is to present an FWI workflow for CZ seismic data.

Applications of FWI to near-surface problems to date have been aimed at a wide diversity of targets, and use a variety of inversion approaches. Some studies have focused on exclusively using body waves to inform shallow subsurface structure. For example, Sheng et al. (2006) used first arrivals to invert for p-wave velocity (Vp) while other researchers have used both P and S body-wave phases to constrain both Vp and shear-wave velocity (Vs) (e.g., Chen et al., 2017; Liu et al., 2021). Others have primarily inverted surface waves for archaeological or engineering applications (e.g., Köhn et al., 2019; Pan et al., 2018; Smith et al., 2019; Wang et al., 2019c) or inverted surface waves extracted from ambient noise data to study CZ structure and weathering (Wang et al., 2019a,b). While this set of prior work informs how FWI can be applied in the CZ, there remain several areas in which major advancements can be made. First, with the exception of Wang et al. (2019a,b), all the aforementioned studies base their forward and adjoint modeling on finite difference methods, which are not well suited to areas with complex topography (e.g., Fichtner, 2010; Komatitsch and Vilotte, 1998). Second, nearly all previous applications of FWI in the CZ focused exclusively on inverting either body or surface waves, but not both, meaning much of the available data was left unused. Third, all of these past works used proprietary codes not readily available to all. Finally, those prior studies were unable to ground truth their methods and results against borehole logs.
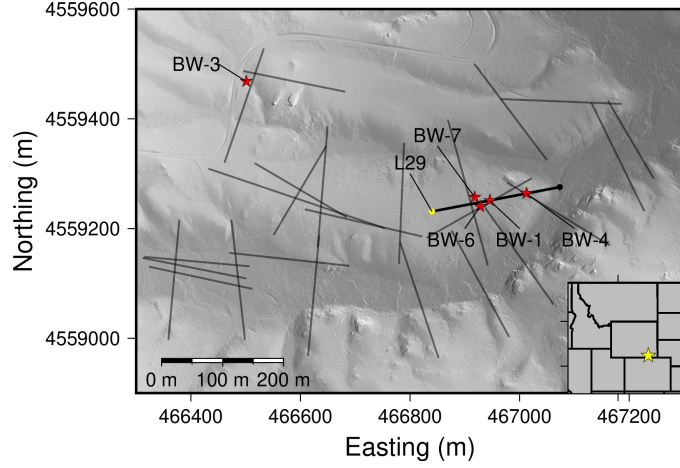
Our work builds on previous applications of FWI in the CZ by creating a workflow that, for the first time, combines all of the following features. First, our workflow enables full elastic wave propagation across complex topography via the spectral element method (e.g., Komatitsch and Tromp, 1999; Komatitsch and Vilotte, 1998). Second, our FWI strategy is informed by sensitivity analyses (e.g., Tape et al., 2010) and tailored to elucidate CZ structure using both surface and body waves. Third, our method is implemented using readily available open-source packages which enable optimized computation via graphics cards on standard workstations (Chow et al., 2020; Komatitsch and Tromp, 1999; Modrak et al., 2018). Finally, we selected a dataset with which we can test our results against data from two boreholes.

The resulting FWI workflow is broadly applicable to the seismic refraction data sets commonly acquired for CZ science. These results bring the CZ community one step closer to routinely imaging subsurface CZ heterogeneity, including weathering profiles, fracture zones, and corestones. In the following sections, we discuss our study site, describe our FWI method and workflow, benchmark the method against synthetic data, present FWI results that show remarkable heterogeneity corroborated by downhole data, and discuss the implications of this work for improving our understanding of CZ processes.

2 Study Site

The Blair Wallis (BW) catchment is located in the Medicine Bow National Forest, $\sim$ 21 km southeast of Laramie, WY. Over the past decade, the site was studied extensively by the Wyoming Center for Environmental Hydrology (WyCEHG). The topography of BW exhibits gently undulating hillslopes (Bradley, 1987; Chapin & Kelley, 1997; Eggler et al., 1969; Evanoff, 1990). BW receives about 620 mm of annual precipitation, most of which ($>$ 90%) is snow, and has a mean annual temperature of 5.4 °C (Natural Resources Conservation Service, 2015). Along the ridges, sagebrush is the dominant vegetation, while aspens, lodgepole pines, and willows appear in topographic lows.

BW is underlain by the Sherman Granite, a sub-unit of the 1.4 GA Sherman Batholith that was uplifted during the Laramide Orogeny (Frost et al., 1999; Peterman & Hedge, 1968; Zielinski et al., 1982). The mineralogical makeup of the coarse-grained Sherman Granite is roughly 40-55 % potassium feldspar, $15 - 30$ % quartz, 20 % plagioclase feldspar, and $5 - 10$ % biotite (Edwards & Frost, 2000; Frost et al., 1999; Geist et al., 1989). While there is no recognizable metamorphic fabric in the rock, a pervasive tectonically induced NE-SW striking fracture population can be observed in outcrops and in aerial imagery. These fractures dip $30 - 80°$ and cause the bedrock and saprolite to exhibit moderate seismic anisotropy (Novitsky et al., 2018).

Figure 1. Hill shade map of the BW study site taken from Flinchum et al. (2022), where various seismic refraction profiles collected by WyCEHG are demarcated with black lines. The seismic refraction profile used in this study is L29. The yellow dot indicates where x = 0 along the transect. The red stars show the locations of boreholes that were drilled and logged. In this work, we show borehole logs from BW1 and BW4 which are located directly on L29.
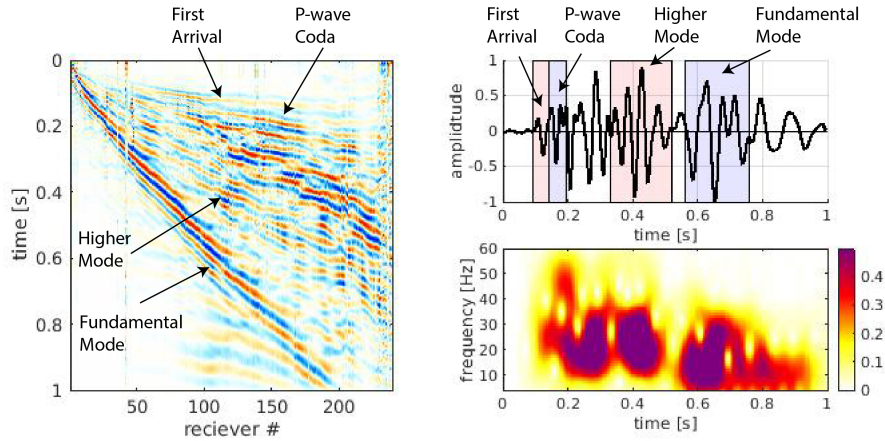
3 Methods

In July 2013, WyCEHG collected a 239-m-long seismic refraction line along a ridge in BW (Figure 1). First arrival traveltimes of these data were manually picked, inverted using FATT, and published first in Flinchum et al. (2018) and later in Flinchum et al. (2022). Our workflow followed these steps, each of which is described in more detail in sections 3.2-3.5 below. First we used the Flinchum et al. (2022) Vp model as the starting Vp model and to estimate source time functions. Second, we constructed an initial Vs model using wave equation dispersion inversion (e.g., Li et al., 2016). Third, we conducted sensitivity analysis of the phases we inverted using the adjoint state method (e.g., Tromp et al., 2005). Finally, we applied FWI to the data using a custom workflow tailored to the challenges of near-surface seismic data.

3.1 Seismic Data

Data used in this study were acquired on a linear array of 240 vertical-component geophones spaced at 1 m intervals and sampled every 500 μs over a record length of 1 s. The frequency response of the geophones increases from 0 – 4.5 Hz and then is vir-

tually flat up to 1,000 Hz. A total of 20 sledgehammer source points generated seismic energy every 12 m along the profile, with one missing source at 24 m.

The recorded waveforms show multiple distinct phases, including first arrival p-waves, a p-wave coda phase directly behind the first arrival, a clear fundamental mode Rayleigh wave phase, and a higher-mode surface wave. The body wave phases display a broader bandwidth with more energy at higher frequencies (8 - 56 Hz), while the surface waves exhibit narrower bands concentrated around lower frequencies (6 - 22 Hz) (Figure 2). In section 3.4 we perform sensitivity analysis on each of the four phases identified in the top right panel of Figure 2.

Figure 2. Left panel: a filtered (5-56 Hz) shot gather from a source located 0 m along the transect. Upper right panel: the geophone recording for the instrument located 120 m along the transect. The first arrival, p-wave coda, higher mode surface wave, and fundamental mode surface wave are highlighted. Each waveform in the highlighted boxes is back-projected to construct the sensitivity kernels in Figure 4. Bottom right panel: a spectrogram of the trace in the upper right panel, showing higher frequencies in the P-wave first arrival and lower frequencies in the Rayleigh wave.
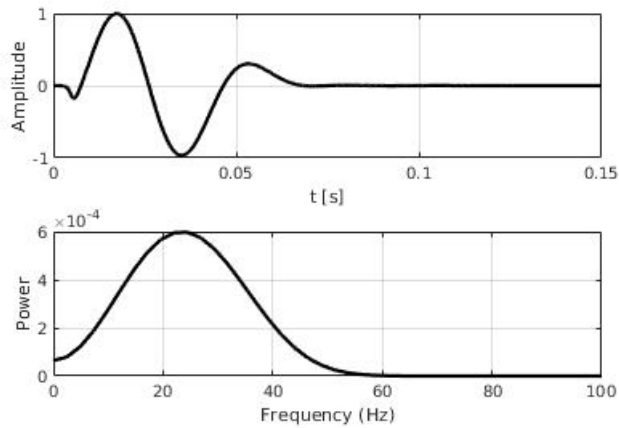
3.2 Source Estimation

Because the source time function (STF) at each hammer location may vary depending on local ground conditions, the individual generating the source, and potentially other

factors (Figure S1), it is necessary to estimate a unique STF at each source location. Because our initial FATT Vp model accurately predicts first arrival times, it is suitable for estimating the STF for each shotpoint, using (e.g., Borisov et al., 2020; Pratt, 1999):

$$s(\omega) = \sum_{i \in window} \frac{u_i^0(\omega) \cdot g_i^*(\omega)}{g_i(\omega) \cdot g_i^*(\omega) + \gamma} \tag{1}$$

In equation (1), i is the index of a particular trace, u^0 is preprocessed observed data, g is preprocessed data modeled using a STF with a unit frequency spectrum, $*$ denotes the complex conjugate, γ is a regularization parameter which also helps avoid division by zero, and s is the estimated STF. For the source estimation, the preprocessing steps include normalizing the waveforms such that the maximum amplitude of each trace is 1 and muting out everything except the first arrivals by applying a time window behind the first arrival pick with a duration of $1/f_0$ where $f_0 = 30$ Hz is roughly the dominant frequency of the data. We only use first arrivals to inform the STF estimates because these are the only phases reliably fit by the FATT model. To minimize near-source effects and to boost signal/noise ratios, we stacked data over offsets of $100 - 175$ m. Using data at these offsets to inform the STF also helps account for some of the unmodelled effects of anelastic attenuation (e.g., Borisov et al., 2020).

Figure 3. The estimated source time function and frequency spectrum for the hammer swing located at x = 0 m.

3.3 Initial Shear-Wave Velocity Model

With an estimate of the STFs in hand, next we built a suitable starting Vs model for FWI. Rather than using a scaled version of the starting Vp model for this purpose (e.g., Liu et al., 2022), we found that a more rigorous prior estimate of the Vs field is necessary to perform FWI on the surface waves. To do this, we leveraged the well-known phenomenon of surface wave dispersion using the wave equation dispersion inversion (WD) technique developed by Li et al. (2016). WD is a skeletonized data inversion strategy, meaning that it uses the same forward and adjoint modeling typically employed in FWI, but fits a significantly smaller portion of the data. While this results in a lower resolution inversion, unlike FWI, the convergence of WD is almost guaranteed.

The WD method minimizes the following functional

$$\chi^{WD} = \frac{1}{2} \sum_{i=1}^{N_s} \int_\omega \Delta\kappa_i(\omega)^2 d\omega \tag{2}$$

where i is the source index, N_s is the number of sources, ω is the angular frequency, and $\Delta\kappa$ is the difference between the dispersion curves of observed and synthetic data. To compute $\Delta\kappa$, two Fourier transforms are performed on the preprocessed synthetic and observed shot gathers, $U(t,x)$ and $U^0(t,x)$, to derive $\tilde{U}(\omega,\kappa)$ and $\tilde{U}^0(\omega,\kappa)$ respectively, transforming the shot gathers from the time-offset domain to the angular frequency-wavenumber domain. Then, for each ω, $\Delta\kappa$ is calculated via cross-correlation such that

$$\Delta\kappa(\omega) = \arg\max_\kappa \mathcal{R}\left\{ \int \tilde{U}(\omega,\kappa') \cdot \tilde{U}^0(\omega,\kappa'+\kappa)\, d\kappa' \right\}, \tag{3}$$
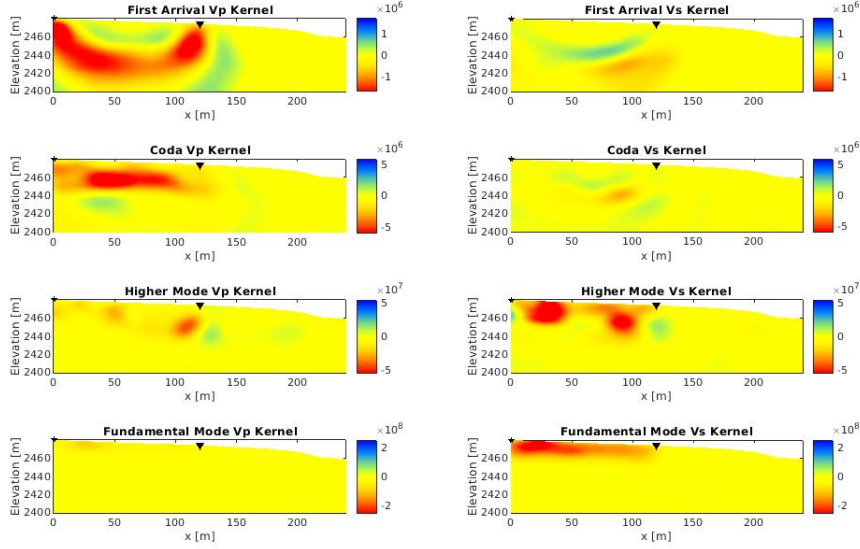
with $\mathcal{R}\{.\}$ taking the real part of a complex number. The preprocessing during the WD inversion involves normalizing all traces and muting data outside the 10 - 75 m offset range. The shear-wave velocity of the starting model for the WD inversion increases linearly with depth. Due to the limited depth sensitivity of the WD method, the lower portion of the final WD model is altered to be a scaled version of the FATT Vp model by a factor of two.

3.4 Sensitivity Analysis

With an initial model parameterized, we can compute the traveltime sensitivity kernels (also known as banana-doughnut kernels or Fréchet Derivatives) of the four read-

226 ily identifiable phases: the first arrival, p-wave coda, higher mode surface wave, and fun-

227 damental mode surface wave (Figure 2). For demonstration purposes, we used the trace

228 and windows shown in the upper right panel of Figure 2 to back project the time-reversed

229 particle velocity at the receiver location through the initial model (e.g., Tromp et al., 2005;

230 Fichtner et al., 2008; Tape et al., 2010) (Figure 4). Repeating this sensitivity analysis

231 on other source-receiver pairs yielded similar results. The sensitivity analysis is an im-

232 portant step in our workflow as it provides insights into which waveforms are useful for

233 updating certain model parameters.

234 For example, the traveltime kernel of the first arrival is characteristic of a diving

235 wave, exhibiting the quintessential banana shape often associated with teleseismic body

236 waves in vertical cross-section (top left panel of Figure 4). Along the ray path, the ker-

237 nel is negative, meaning that a decrease in the wave speed will result in an increase in

238 traveltime (e.g., Tromp et al., 2005). The traveltime kernel of the first arrival has a wide

239 sensitivity zone, indicating a broad depth range determines the diving wave arrival time.

240 The p-wave coda, in contrast, appears to travel primarily in the near-surface and is sen-

241 sitive to a narrower depth range (second row of Figure 4). Regardless of the paths the

242 energy takes, both types of body waves are primarily sensitive to Vp (Figure 4). The fun-

243 damental mode Rayleigh wave traveltime is primarily sensitive to the upper 15 – 20 m,

244 while the higher mode Rayleigh wave shows a more complicated sensitivity kernel, with

245 deeper and shallower sensitivity where energy focuses and defocuses respectively (third

246 and last rows Figure 4 respectively). Although other clear phases exist in the vertical-

247 component data (Figure 2), we were unable to use sensitivity analysis to confirm that

248 any of these arrivals are shear or converted body waves. However, our method is appli-

249 cable to such phases if observed.

Figure 4. Sensitivity kernels with respect to each model parameter (Vp and Vs) for each of the four highlighted phases in the upper right panel of Figure 2. The first column corresponds to sensitivity with respect to Vp, while the second column corresponds to sensitivity with respect to Vs. The first row shows the sensitivity of the first arrival, the second row shows the sensitivity of the p-wave coda, the third row shows the sensitivity of the higher mode surface wave, and the last row shows the sensitivity of the fundamental mode surface wave.

3.5 Full-Waveform Inversion Workflow

In this study, we used a fork of the FWI workflow manager SeisFlows published by Modrak et al. (2018), which primarily serves as a wrapper for the forward and adjoint (an)elastic wavefield solver, specfem2d (Komatitsch and Tromp; 1999). The use of the spectral element method in this study is particularly important given the topographic variation in the ground surface of our model. Specifically, the free surface boundary condition at the ground surface is rigorously fulfilled by the spectral element method, unlike in other modeling strategies, such as grid-based finite difference methods (e.g., Fichtner, 2010).

During the FWI portion of our workflow, we defined the functional to be minimized, χ, using the normalized correlative (NC) misfit norm,

$$\chi = \frac{1}{N_s \cdot N_r} \sum_{i=1}^{N_s} \sum_{j=1}^{N_r} \left[1 - \int_T \hat{u}_{i,j} \cdot \hat{u}_{i,j}^0 \; dt \right], \tag{4}$$

where $\hat{u}$ and $\hat{u}^0$ are synthetic and observed waveforms with their maximum amplitudes normalized to 1, N_s is the number of sources, and N_r is the number of receivers. $\int_T \hat{u}_{i,j} \cdot \hat{u}_{i,j}^0 \; dt$ is called the correlation coefficient and measures the similarity of two time series. We chose the NC norm because it is both noise-resistant and emphasizes fitting phase rather than amplitude (e.g., Borisov et al., 2020; Choi and Alkhalifah, 2012). This helps contend with noise in the data as well as certain unmodelled anelastic and 3D effects (e.g., Borisov et al., 2020). To minimize the NC norm, we iteratively update the velocity model, $\boldsymbol{m}$, according to

$$\boldsymbol{m}^{i+1} = -\alpha \boldsymbol{P} \boldsymbol{H} \nabla_{\boldsymbol{m}} \chi + \boldsymbol{m}^i \tag{5}$$

In the above equation, $\nabla_m \chi$, the gradient with respect to the misfit functional, χ, is computed via the adjoint method, α is a step length computed via a bracket line search, and $\boldsymbol{P}$ is a diagonal preconditioning matrix containing the discretized field P_1^{-1} which is defined as

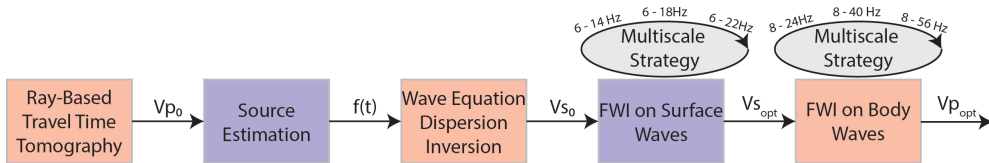$$P_1(x,z) := \sum_{i=1}^{N_s} \int_T \partial_t^2 u_i(x,z) \cdot \partial_t^2 u_i(x,z) \; dt \tag{6}$$

where $u_i(x,z)$ is the synthetic wavefield excited by the ith STF. The main purpose of the preconditioner is to remove numerical artifacts caused by large amplitudes near the ground surface and to account for the geometric spreading of the wavefield. In equation 5, $\boldsymbol{H}$ is the Hessian matrix; in practice, we approximate the Hessian-gradient product, $\boldsymbol{H} \nabla_{\boldsymbol{m}} \chi$, using a limited-memory Broyden–Fletcher–Goldfarb–Shanno algorithm (Liu and Nocedal, 1989). We used the same modeling strategy and optimization framework for the WD step of our workflow.

The FWI strategy used in this study was informed by our preliminary analysis of the data. We inverted surface waves and body waves separately, in different steps of the workflow, because the sensitivity with respect to surface waves is about two orders of magnitude higher than the sensitivity with respect to body waves (Figure 4). Hence it would require extreme scaling of the body waves to balance their contributions to model updates with those of the surface waves, which creates numerical artifacts. Separating

the surface and body waves is also advantageous because of their different frequency contents. Using a multiscale approach (e.g, Bunks et al., 1994; Chen et al., 2019), we work through the frequency content of the surface waves gradually, focusing on their lower frequencies, while we step through frequencies of the body waves more aggressively to cover their wider bandwidth.

With these issues in mind, we chose to invert the surface waves first, using them to inform the upper portion of the earth model. Then, in a quasi-layer-stripping approach, we updated the deeper part of the model using the body waves. During the surface wave step of the workflow, both Vp and Vs are updated, while only Vp is updated during the body wave step because the first arrivals and p-wave coda are primarily sensitive to Vp (Figure 4). We found that any Vs sensitivity shown in computed Fréchet derivatives for the first arrival or p-wave coda is likely a numerical artifact that degrades the fit of surface waves if incorporated into the model updates derived from the body waves (Figure 4).

The preprocessing of waveforms in both steps included muting traces outside a particular offset range, bandpass filtering, normalizing all traces to a maximum amplitude of 1, and muting various arrivals. In the surface wave inversion step, traces between 10 − 150 m offset were used, with 6 − 14, 6 − 18, and 6 − 22 Hz bandpass filters applied, while all phases arriving earlier than the higher mode were muted. In the body wave step, traces between 50 − 210 m offset were used, with 8 − 24, 8 − 40, and 8 − 56 Hz bandpass filters applied, and all phases arriving later than the p-wave coda were muted. To regularize the inversions, we smoothed the gradients by convolving them with a 2D Gaussian function. In the surface wave step, we used a smoothing radius of 10 m for all stages of the multiscale strategy, while for the body wave step, we used smoothing radii of 40, 20, and 10 m, decreasing the smoothing radius as we increased the frequency content during each stage of the multiscale strategy.
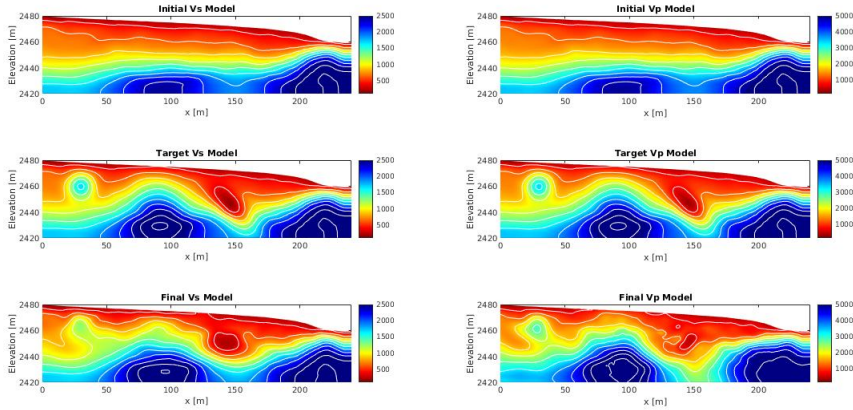

Figure 5. A flow chart of our FWI strategy showing both preliminary steps and FWI stages.

4 Results

4.1 Workflow Validation with Synthetic Data

We benchmarked the FWI portion of our workflow (the last two boxes in Figure 5) by inverting synthetic data to illustrate the kinds of features that can be recovered. For this synthetic test, we used the same survey geometry and starting Vs and Vp models as in our real data case, but added three velocity anomalies: a shallow high-velocity anomaly representing a corestone, a deeper high-velocity anomaly indicative of an area of bedrock with low fracture density, and a low-velocity zone characteristic of a fracture zone. Generally speaking, our FWI workflow recovers all three anomalies fairly well, although the shape of anomalies in the final models is not perfect (Figure 6). Nonetheless, this synthetic test bolsters confidence that we can trust relatively large-scale features (on the order of 10 m or larger) in our FWI results.
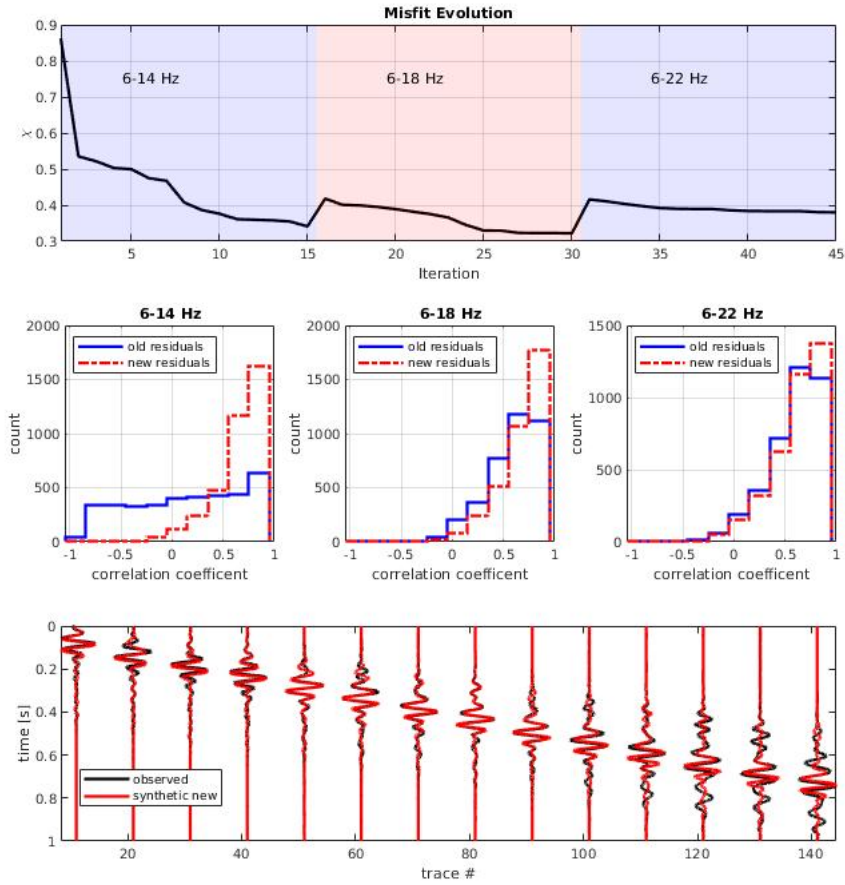

Figure 6. Results from the synthetic FWI experiment. The left column has Vs models and the right column has Vp models. The first row shows the starting models, the second row shows the target models, and last row shows the inverted models. Velocity contours on the Vs and Vp models have intervals of 250 m/s and 500 m/s respectively.

4.2 Surface Wave Step

After the FATT, source estimation, and WD, the low-frequency (6 – 14 Hz) surface wave data tends to fit within one wavelength but is not yet perfectly recovered (Fig-
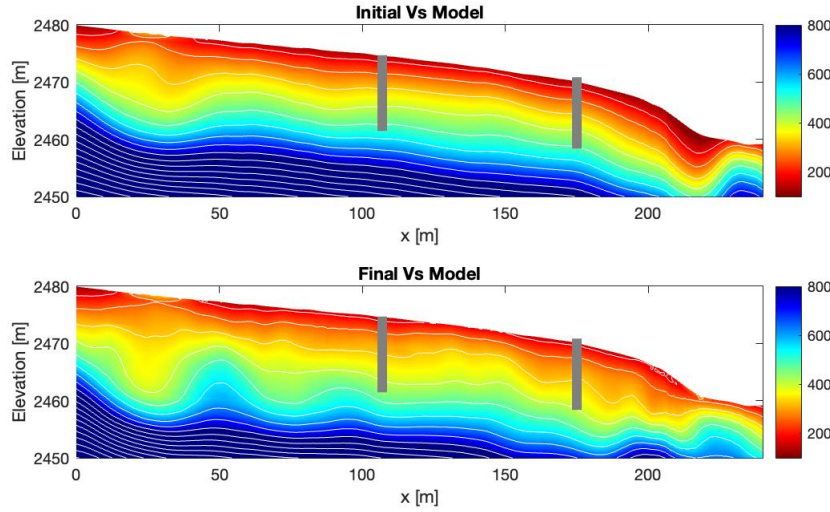
³¹³ ure S2). By the end of the first stage of the surface wave inversion, the phase informa-

³¹⁴ tion of Rayleigh waves is well represented by synthetics (Figures 7 and S2). In the lat-

³¹⁵ ter two stages, higher frequency data is progressively fit (6 – 18 Hz and 6 – 22 Hz). In

³¹⁶ these stages, only relatively small adjustments to the synthetic waveforms are needed

³¹⁷ to improve the model fits (Figures 7, S3, and S4). Generally speaking, as the frequency

³¹⁸ content of the data being fit increases, diminishing returns in decreasing the misfit func-

³¹⁹ tion are made (Figure 7).

Figure 7. Top panel: The evolution of the misfit function with each FWI iteration, segmented by each stage of the multiscale strategy. Middle panels: histograms of the the correlation coefficients, $\int_T \hat{u}\hat{u}^0 dt$, for all traces before and after each stage of the multiscale strategy. Bottom panel: Prepossessed (body waves are muted and 6 - 22 Hz bandpass filtered) waveforms after surface wave FWI.
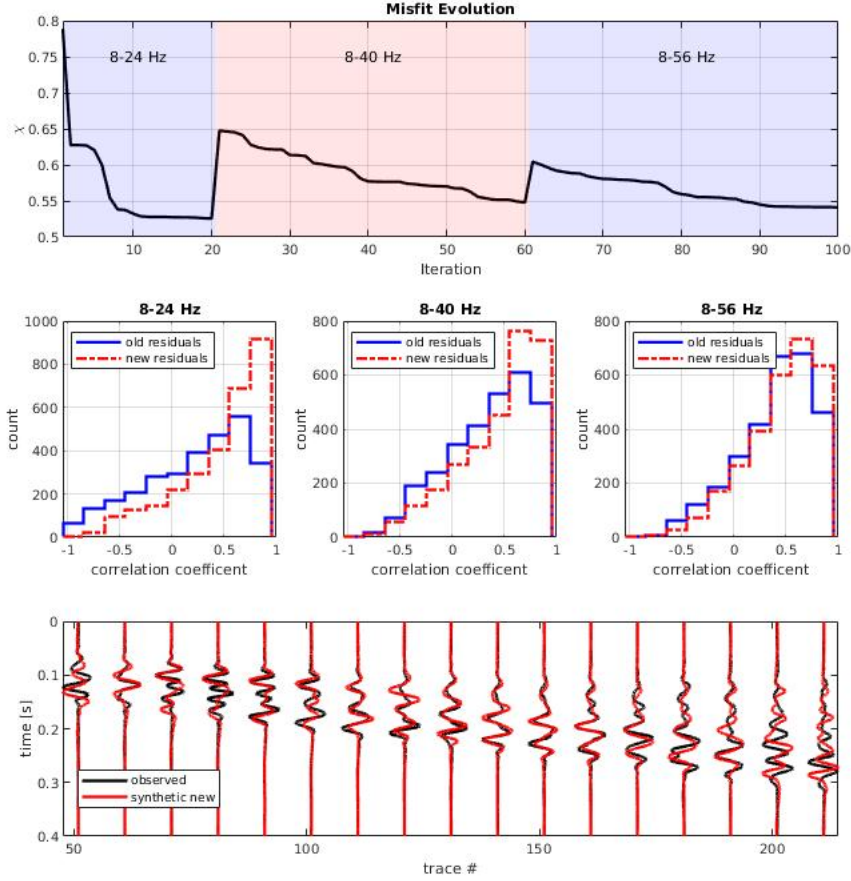
³²⁰   In the resultant Vs model, we observe several features indicative of the increased

³²¹ resolution gained by performing FWI using surface waves (Figure 8). One such feature

³²² is a high-velocity zone around x = 50 m, where the 400 – 600 m/s velocity contours are

³²³ bowed upward. The strongest vertical velocity gradients occur towards the far end of the

³²⁴ line (x = 210 – 239 m). Note that the casing depths of the two boreholes correspond with

³²⁵ shear-wave velocities of 400 - 500 m/s, suggesting that these velocities may be a good

³²⁶ range to use for inferring the boundary between saprolite and fractured bedrock.

Figure 8.   Shear-wave velocity models before and after FWI. Velocity contours at 75 m/s intervals are also shown in white. The gray rectangles show the locations of borehole casings. Please note the limited elevation range of these plots.
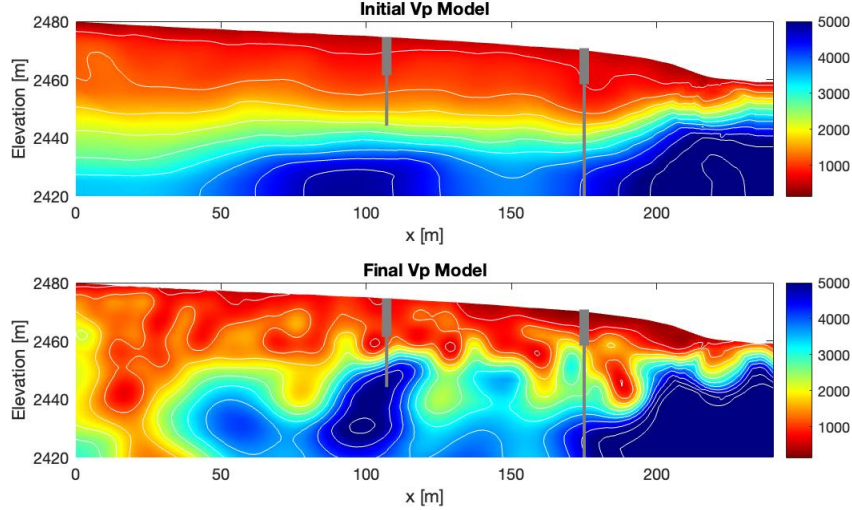
4.3 Body Wave Step

³²⁸   At the onset of the first stage of the multiscale strategy for the body waves, the

³²⁹ low-frequency (8 – 24 Hz) data tends to fit reasonably well, implying that the FATT model

³³⁰ and STF estimates provide a good initial parameterization for performing FWI (Figure

³³¹ S5). In the ensuing stages of the multiscale strategy, we see that both the p-wave coda

³³² and first arrival are accurately fit by the synthetics, although the data fit degrades slightly

³³³ at offsets greater than 200 m (Figures 9, S5, S6, and S7). Convergence was slower for

³³⁴ the body waves and required more iterations than during the surface wave step (Figure

³³⁵ 9).

Figure 9. Top panel: The evolution of the misfit function with each FWI iteration, segmented by each stage of the multiscale strategy. Middle panels: histograms of the the correlation coefficients, $\int_T \hat{u}\hat{u}^0 dt$, for all traces before and after each stage of the multiscale strategy. Bottom panel: Prepossessed (surface waves are muted and 8 - 56 Hz bandpass filtered) waveforms after body wave FWI.

In the final Vp model, large updates can be observed, showing the impact of applying FWI to the body waves (Figure 10). Several novel features are observed in the final Vp model, including a high-velocity zone located at around 100 m, deep low-velocity zones located around x = 20 and 190 m, and various fine structures in the near-surface. Generally speaking, vertical and lateral velocity gradients have increased substantially in several areas. Interestingly, there appears to be more near-surface heterogeneity in

the final Vp model than in the Vs model, and we discuss why this may be the case in section 5.1. Several of the features we have noted were also observed by Wang et al. (2019b), including deep low-velocity zones and more heterogeneity in Vp relative to Vs.
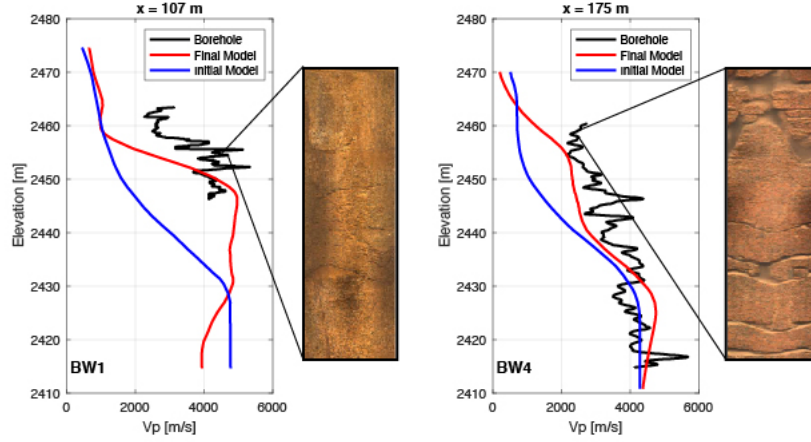

Figure 10. P-wave velocity models before and after FWI. Velocity contours at 500 m/s intervals are also shown in white. The gray rectangles show the locations of borehole casings, while the gray lines show where the borholes were logged.

4.4 Comparison to Borehole Data

Two boreholes on our profile, BW1 and BW4, located at roughly x = 107 and 175 m, provide an opportunity to ground-truth our FWI results. As summarized in Flinchum et al. (2022), the upper parts of the boreholes drilled through incompetent soil and saprolite were cased, and the deeper open holes were logged. Since no borehole data from the saprolite and soil exist, we cannot compare borehole logs with the surface wave Vs models where only the upper $\approx$ 20 m or so are constrained (Figure 4). The borehole logs are, however, an effective ground truth for the Vp models, where the diving wave provides information on deep CZ structure (Figure 4).

The final Vp model shows much better agreement with the borehole logs than the initial model, demonstrating substantial gains from FWI (Figure 11). While the initial model created using FATT is far too smooth and incorrectly estimates velocities at moderate depth (15 − 30 m), after applying FWI, this inconsistency is greatly reduced. This

comparison suggests that FATT may underestimate vertical velocity gradients in the CZ (Figures 10 and 11). The borehole comparison suggests that both the high-velocity and low-velocity zones in our final Vp model are true features rather than inversion artifacts. Although these low-velocity zones have not been directly observed in either borehole presented, the aforementioned synthetic tests support that we can recover such features using our FWI workflow.

Figure 11. Comparison of the FATT and FWI Vp models with the borehole logs from BW1 (left) and BW4 (right) and expanded views of the bedrock observed in optical logs over a 2 m depth range in each hole. Note higher fracture density visible in BW-4, which corresponds to lower P-velocities in that hole.

5 Discussion

5.1 Limitations, Uncertainties, and Outlook on Future Work

While our results are promising, some areas of improvement exist for our methodology, including potentially incorporating 3D modeling to more accurately recover geometric wavefield spreading. While more rigorous, incorporating 3D modeling would likely require a supercomputing cluster (e.g., Chow et al., 2020; Wang et al., 2019a; Wang et al., 2019b), whereas limiting the technical overhead of FWI by implementing it on a workstation, as we have, makes the method accessible to more researchers. Furthermore, given our exclusive use of phase information and focus on inverting for velocity, incorporating 3D modeling may not significantly change our results. It is more likely that the biggest

gains achieved by incorporating 3D modeling would also require full 3D data coverage (Górszczyk et al., 2023), allowing us to recover the true 3D structure of Earth's CZ. For these reasons, we leave 3D modeling for future work.

Other areas of improvement for our workflow pertain to our parameterization of the Earth model. For example, including a reasonable estimate of anelasticity may help limit inversion artifacts (e.g., Borisov et al., 2020; Groos et al., 2014). In particular, we expect anelasticity to affect the surface wave inversion to a greater extent than it would the body wave inversion, as the surface waves travel significantly more cycles than the body waves. Nonetheless, given the complexities of parameterizing or inverting for a dynamic and heterogeneous near-surface anelasticity field (Askan et al., 2007), we leave this issue for future work. We also do not rigorously parameterize or invert for density in our workflow. In our modeling, density is set as an arbitrary scalar so that Vp and Vs fields can be converted to Lame parameters for input into specfem2d. Changes in our parameterization of the density field could affect the amplitudes of synthetic waveforms (e.g., Liu et al., 2022). However, since we exclusively use phase information in our inversion and normalize all the traces, changes in our representation of density should have little to no effect on our final results. Given the inconsistent coupling of instruments in the data set we used, attempting to use amplitude information to constrain density would likely be ill-conceived, although future advances in instrumentation may someday make this a worthwhile pursuit (e.g., Yuan et al., 2015). Additionally, since CZ materials may exhibit significant seismic anisotropy (Eppinger et al., 2021; Novitsky et al., 2018), accounting for anisotropy may further improve FWI results, although this would likely require some prior information about the anisotropy of the study site or 3D, multi-component data coverage (e.g., Toyokuni and Zhao, 2021).

Another limitation in our FWI models relates to what extent the separately inverted Vp and Vs fields can be used to calculate Poisson's ratio in the CZ, given that the Vp FWI model is significantly more heterogeneous than the Vs model (Figures 8 and 10). It is possible that the contrast in Vp vs. Vs heterogeneity is caused by variations in the fluid content of the pore spaces, since shear velocity is insensitive to water saturation. Another possible explanation is that the information contained in the surface waves varies from that of the body waves. Considering that anelasticity usually correlates with velocity (e.g., Asian et al., 2007; Borisov et al., 2020), the surface waves traveling primarily through lower-velocity material likely attenuate more than the body waves. This would

result in the surface waves having a lower frequency content (e.g., Figure 2) and may cause models derived with them to lack high-wavenumber information. Alternatively, the Vp model may contain excess heterogeneity, namely inversion artifacts caused by the lower signal-to-noise ratio of the body waves. We think it would be constructive for future work to investigate which of these possible explanations is most plausible.

Future work could also make various theoretical advancements to our FWI workflow. For example, using source encoding could significantly reduce the computational cost of FWI in the CZ or reserve computational resources for incorporating 3D modeling and more data into workflows (e.g., Tromp and Bachman, 2019). More investigation into which misfit function is best for FWI in the CZ would be beneficial. Looking into measurements that limit errors associated with source estimation and instrument response while simultaneously increasing resolution, such as the double difference measurement (e.g., Yuan et al., 2016) would be worthwhile. Trialing other misfit functions that capture traveltime differences of multiple events, such as the local traveltime inversion method proposed by Hu et al., (2020) could also be advantageous. Another promising branch of research is uncertainty quantification for FWI in the CZ, as these methods may help researchers to identify and avoid interpreting inversion artifacts (e.g., Thurin et al., 2019).

5.2 Implications for Critical Zone Heterogeneity

One of the primary challenges in capturing and characterizing critical zone processes is the vast range in scales they span. At the smallest scales, chemical weathering occurs at the molecular and grain scale, driven by chemical reactions on individual mineral surfaces, often aided by symbiotic fungi at the micron scale (e.g., Brantley et al., 2017; Navarre-Sitchler et al., 2015; Sak et al., 2010). At larger scales, we might expect weathering to depend on climatic patterns that can vary at regional or watershed scales (e.g., Goodfellow et al., 2013). Other processes might be relevant at intermediate scales, including compositional heterogeneity, fracture zones, slope-aspect contrasts, or bedrock foliation (Callahan et al., 2022; Eppinger et al., 2021; Leone et al., 2020; Novitsky et al., 2018; West et al., 2019). This diverse set of processes acting across multiple scales creates heterogeneity in subsurface CZ structure, which is visible in outcrops (e.g., Dethier and Lazarus, 2006), corestones (Sak et al., 2010), and thin sections (e.g., Holbrook et al., 2019). Capturing such heterogeneity in the subsurface critical zone is a formidable challenge, for which improved geophysical methods like FWI are needed.

Our results show that critical zone structure is laterally heterogeneous at scales much smaller than can be attributed to large-scale forcing functions like climate or tectonic stress. For example, the depth at which fast velocities associated with intact bedrock (Vp > ~4000 m/s) is reached varies by more than a factor of two over only 15 m horizontal distance, from ~20 m at x = 110 m to greater than 50 m at x = 125 m (Fig. 10). Over that same stretch, the thickness of the weathered bedrock layer (1,200 m/s < Vp < 4,000 m/s) goes from only a few meters to more than 25 m. Contrasts at this horizontal scale cannot be the consequence of differing climate, and given the location of this profile along a ridgeline, it is similarly difficult to imagine other top-down processes (e.g., hydrology, vegetation) could produce such variability. Instead, we must seek bottom-up explanations for these changes, sourced in the local geology (e.g., composition or fractures).

Both the boreholes and the details of the FWI inversion provide clues as to the causes of these strong lateral contrasts in critical zone structure. In particular, the drilling results at BW1 and BW4 combined with the FWI velocity model tell a story of two distinct weathering fronts at these locations. At BW1, we observe strong vertical velocity gradients in both the borehole log and FWI model and very few open fractures in the underlying bedrock (Figure 11). Meanwhile, at BW4, the vertical velocity gradients in the borehole log and FWI model are more diffuse, and more intensely fractured bedrock exists at depth. These results imply that the sharpness of the transition from weathered to unweathered materials depends on the fracture density of bedrock as it enters the CZ weathering engine. Indeed, the thickness of the fractured bedrock layer appears to be inversely correlated with the velocity of the underlying bedrock. In parts of the model with very fast (> 4,500 m/s) bedrock velocities, there is a rapid transition to overlying saprolite, with little (or no?) weathered bedrock, while elsewhere slower deep bedrock underlies thick weathered bedrock layers – suggesting a bottom-up control on CZ architecture here (Figure 10). Such bottom-up controls could include lateral changes in composition (e.g., Brantley et al., 2017; Basilevskaya et al., 2013), foliation (Leone et al., 2020), or fracture density (e.g., Novitsky et al., 2018). At our site, we suggest that changes in bedrock fracture density are most likely, given the observation of fracture zones in adjacent outcrops.
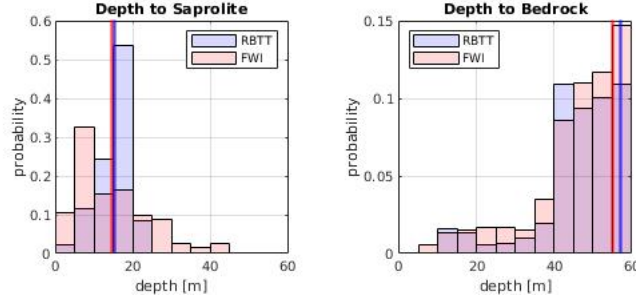
Additional intriguing features in the FWI model include narrow, steeply dipping zones of very low velocity (< 1,000 m/s) that penetrate tens of meters into the subsur-

face at several places along the line (e.g., at x ≈ 25 m and x ≈ 185 m). These features might represent deep zones of intense chemical weathering and fracturing. While our boreholes were not placed to verify the presence of these features, such low-velocity zones might well play an outsized role in guiding water through the subsurface. Thus, full-waveform inversion promises to yield important new insights into catchment hydrology.

Given that the full waveform results show such heterogeneity, does this imply that the ray-based tomograms that have been the primary seismic tool for imaging the critical zone are wrong? To address this, we compared our FWI results with the FATT initial model. At a glance, the FWI model is much more detailed and heterogeneous than the FATT model (Figure 10). A comparison of the depth ranges of velocities associated with the saprolite-bedrock transition (1.2 km/s), however, reveals that while the depths distributions are more variable in the FWI model, the average saprolite thicknesses are similar in the FWI and FATT results (Figure 12). The same can be said for the depth to intact bedrock (Figure 12). Thus, FATT accurately captures long-wavelength features in the CZ but misses smaller-scale heterogeneity. That is to say, FATT models aren't wrong, but they are blurry. This point is further emphasized by the upper left panel of Figure 4, showing the banana-doughnut kernel for the first arrival. The large volume of the kernel implies that first arrival traveltimes are sensitive to the average velocity of a significant portion of the subsurface, and this detail is reflected in the blurriness of FATT models. These findings help contextualize previous conclusions based on FATT models, which have elucidated large-scale, first-order controls on CZ structure such as slope aspect (Befus et al., 2011), regional tectonic stresses (St. Clair et al., 2015), and foliation (Leone et al., 2020). Our findings show that FWI can build on this past research by unearthing the effects of smaller-scale processes. In other words, the average saprolite thickness at a site may reflect large-scale controls like climate or tectonic stress, while smaller-scale lateral heterogeneity must have local causes, like variations in fracture density or composition.

Figure 12. Overlain histograms of the depth to saprolite (left) and intact bedrock (right) in the FWI (red) and FATT (blue) models. The thick vertical lines indicate averages of the distributions displayed in the histograms.

Our results raise fundamental questions about the extent to which CZ architecture is controlled by large-scale forcing functions like climate, topography, and tectonic stress, versus local, smaller-scale characteristics of the bedrock. While past work has provided useful theories for the role of large-scale processes on CZ structure, our results suggest that smaller-scale factors also play an important role, as variability in bedrock characteristics over lateral scales of tens of meters imparts profound impacts on the overlying CZ architecture. We anticipate a concordance between the scale of forcing functions and their products. Seeking the signal of top-down processes like climate in CZ architecture will thus likely require comparing larger-scale averages across sites to filter out local variability (e.g., Callahan et al., 2022). We expect that future applications of the FWI workflow developed here will provide both new ideas and new hypothesis tests about the state and evolution of Earth's critical zone.

6 Conclusions

In this study, we present an FWI workflow specifically tailored to study weathering patterns in the CZ. Using existing and accessible open source packages, we show how forward and adjoint modeling rooted in the spectral element method can be used to invert surface and body waves to constrain Vs and Vp. Our FWI results agree significantly better with borehole data than previously published FATT models. This, along with synthetic FWI experiments, bolsters confidence in our findings, which show remarkable heterogeneity in the CZ, previously undetectable using traveltime tomography. We hypoth-

esize that local heterogeneity in Earth's weathering engine reflects local variations in bedrock composition and structure, including fracture density, foliation, and mineralogy. We suggest that FWI can be used to investigate a wide range of important CZ processes at smaller scales than previously possible.

7 Open Research

All seismic data and borehole logging data have been uploaded to a Zenodo repository (https://doi.org/10.5281/zenodo.8219762) and MATLAB codes for source estimation as well as a copy of our fork of SeisFlows will be uploaded pending acceptance of this.

Citations:

Askan, A., Akcelik, V., Bielak, J., and Ghattas, O. (2007). Full waveform inversion for seismic velocity and anelastic losses in heterogeneous structures. *Bulletin of the Seismological Society of America*, 97(6), 1990–2008. https://doi.org/10.1785/0120070079

Befus, K. M., Sheehan, A. F., Leopold, M., Anderson, S. P., and Anderson, R. S. (2011). Seismic constraints on critical zone architecture, Boulder Creek watershed, Front Range, Colorado. *Vadose Zone Journal*, 10(4), 1342–1342. https://doi.org/10.2136/vzj2010.0108er

Bazilevskaya, E., Lebedeva, M., Pavich, M., Rother, G., Parkinson, D. Y., Cole, D., & Brantley, S. L. (2013). Where fast weathering creates thin regolith and slow weathering creates thick regolith. *Earth Surface Processes and Landforms*, 38(8), 847–858. https://doi.org/10.1002/esp.3369

Borisov, D., Gao, F., Williamson, P., & Tromp, J. (2020). Application of 2D full-waveform inversion on exploration land data. *GEOPHYSICS*, *85*(2). https://doi.org/10.1190/geo2019-0082.1

Bradley, W. C. (1987). Erosion surfaces of the Colorado Front Range: A review. In W. L. Graf (Ed.), Geomorphic systems of North America (pp. 215–220). Boulder, CO: *Geologic Society of America.*

Brantley, S. L., Eissenstat, D. M., Marshall, J. A., Godsey, S. E., Balogh-Brunstad, Z., Karwan, D. L., Papuga, S. A., Roering, J., Dawson, T. E., Evaristo, J., Chadwick, O., McDonnell, J. J., and Weathers, K. C. (2017). Reviews and syntheses: On the roles trees play in building and plumbing the Critical Zone. *Biogeosciences*, 14(22), 5115–5142. https://doi.org/10.5194/bg-14-5115-2017

Brantley, S. L., Goldhaber, M. B., & Ragnarsdottir, K. V. (2007). Crossing disciplines and scales to understand the critical zone. *Elements*, 3, 307–314. https://doi.org/10.2113/gselements.3.5.307

Bunks, C., Saleck, F. M., Zaleski, S., & Chavent, G. (1995). Multiscale seismic waveform inversion. *GEOPHYSICS*, 60(5), 1457–1473. https://doi.org/10.1190/1.1443880

Callahan, R. P., Riebe, C. S., Sklar, L. S., Pasquet, S., Ferrier, K. L., Hahm, W. J., Taylor, N. J., Grana, D., Flinchum, B. A., Hayes, J. L., and Holbrook, W. S. (2022). Forest vulnerability to drought controlled by bedrock composition. *Nature Geoscience*, 15(9), 714–719. https://doi.org/10.1038/s41561-022-01012-2

Callahan, R. P., Riebe, C. S., Pasquet, S., Ferrier, K. L., Grana, D., Sklar, L. S., et al. (2020). Subsurface weathering revealed in hillslope-integrated porosity distributions. *Geophysical Research Letters*, 47, e2020GL088322. https://doi.org/10.1029/2020GL088322

Chapin, C. E., & Kelley, S. A. (1997). The Rocky Mountain erosion surface in the Front Range of Colorado. In D. W. Bolyard & S. A. Sonnenberg (Eds.), Geologic history of the Colorado Front Range (pp. 1943–3048). Denver, CO: *Rocky Mountain Association of Geologists*.

Chen, J., Zelt, C. A., and Jaiswal, P. (2017). Detecting a known near-surface target through application of frequency-dependent traveltime tomography and full-waveform inversion to P- and SH-wave seismic refraction data. *GEOPHYSICS*, 82(1). https://doi.org/10.1190/geo2016-0085.1

Chen, G. X., Wu, R. S., & Chen, S. C. (2019). Multiscale direct envelope inversion: Algorithm and methodology for application to the salt structure inversion. *Earth and Space Science*, 6, 174–190. https://doi.org/10.1029/ 2018EA000453

Choi, Y., & Alkhalifah, T. (2012). Application of multi-source waveform inversion to marine streamer DATA USING THE GLOBAL CORRELATION NORM. *Geophysical Prospecting*, *60*(4), 748–758. https://doi.org/10.1111/j.1365-2478.2012.01079.x

Chow, B., Kaneko, Y., Tape, C., Modrak, R., & Townend, J. (2020). An automated workflow for adjoint tomography Waveform misfits and synthetic inversions for the north Island, New Zealand. *Geophysical Journal International*, 223(3), 1461–1480.

Dawson TE, Hahm WJ, Crutchfield-Peters K (2020) Digging deeper: what the critical zone perspective adds to the study of plant ecophysiology. *New Phytol* 226(3):666–671

Dethier, D. P., & Lazarus, E. D. (2006). Geomorphic inferences from regolith thickness, chemical denudation and CRN erosion rates near the glacial limit, Boulder Creek catchment and vicinity, Colorado. *Geomorphology*, *75*(3-4), 384-399. https://doi.org/10.1016/j.geomorph.2005.07.029

Eggler, D., Larson, E., & Bradley, W. (1969). Granites grusses and the Sherman erosion surface, southern Laramie Range Colorado-Wyoming. *American Journal of Science*, 267(4), 510–522. https://doi.org/10.2475/ajs.267.4.510

Eppinger, B. J., Hayes, J. L., Carr, B. J., Moon, S., Cosans, C. L., Holbrook, W. S., et al. (2021). Quantifying depth- dependent seismic anisotropy in the critical zone enhanced by weathering of a Piedmont schist. *Journal of Geophysical Research: Earth Surface*, 126, e2021JF006289. https://doi. org/10.1029/2021JF006289

Evanoff, E. (1990). Early Oligocene paleovalleys in southern and central Wyoming: Evidence of high local relief on the late Eocene unconformity. *Geology*, 18(5), 443–446. https://doi.org/10.1130/0091-7613(1990)018%3C0443:EOPISA%3E2.3.CO;2

Fichtner, A., Kennett, B. L., Igel, H., & Bunge, H.-P. (2008). Theoretical background for continental- and global-scale full-waveform inversion in the time-frequency domain. *Geophysical Journal International*, *175*(2), 665–685. https://doi.org/10.1111/j.1365-246x.2008.03923.x

Fichtner, A. (2011.). *Full seismic waveform modeling and inversion*. Springer.

Flinchum BA, Holbrook WS and Carr BJ (2022) What Do P-Wave Velocities Tell Us About the Critical Zone? *Front. Water* 3:772185. doi: 10.3389/frwa.2021.772185

Flinchum, B. A., Holbrook, W. S., Rempe, D., Moon, S., Riebe, C. S., Carr, B. J., et al. (2018). Critical zone structure under a granite ridge inferred from drilling and three-dimensional seismic refraction data. *Journal of Geophysical Research: Earth Surface*, 123, 1317–1343. https://doi.org/10.1029/2017jf004280

Frost, C. D., Frost, B. R., Chamberlain, K. R., & Edwards, B. R. (1999). Petrogenesis of the 1.43 Ga Sherman batholith, SE Wyoming, USA: A reduced, rapakivi-type anorogenic granite. *Journal of Petrology*, 40(12), 1771–1802. https://doi.org/10.1093/petroj/40.12.1771

Goodfellow, B. W., Chadwick, O. A., & Hilley, G. E. (2013). Depth and character of rock weathering across a basaltic-hosted climosequence on Hawaiʻi. *Earth Surface Processes and Landforms*, 39(3), 381–398. https://doi.org/10.1002/esp.3505

Górszczyk, A., Brossier, R., & Métivier, L. (2023). The Impact of the 3D Effect on the Regional-Scale Velocity Model Building Using 2D Full-Waveform Inversion. *European Geophysical Union General Assembly.* https://doi.org/10.5194/egusphere-egu23-4387

Groos, L., Schäfer, M., Forbriger, T., & Bohlen, T. (2017). Application of a complete workflow for 2D elastic full-waveform inversion to recorded shallow-seismic Rayleigh Waves. *GEOPHYSICS*, *82*(2). https://doi.org/10.1190/geo2016-0284.1

Hahm, W. J., Rempe, D. M., Dralle, D. N., Dawson, T. E., Lovill, S. M., Bryk, A. B., et al. (2019). Lithologically controlled subsurface critical zone thickness and water storage capacity determine regional plant community composition. *Water Resources Research*, 55. https:// doi.org/10.1029/2018WR023760

Hahm, W. J., Riebe, C. S., Lukens, C. E., & Araki, S. (2013). Bedrock composition regulates mountain ecosystems and landscape evolution. *Proceedings of the National Academy of Sciences*, 111(9), 3338–3343. https://doi.org/10.1073/pnas.1315667111

Hayes, J. L., Riebe, C. S., Holbrook, W. S., Flinchum, B. A., & Hartsough, P. C. (2019). Porosity production in weathered rock: Where volumetric strain dominates over chemical mass loss. *Science Advances*, 5(9), eaao0834. https://www.science.org/doi/10.1126/sciadv.aao0834

Holbrook, W. S., Marcon, V., Bacon, A. R., Brantley, S. L., Carr, B. J., Flinchum, B. A., et al. (2019). Links between physical and chem- ical weathering inferred from a 65-m-deep borehole through Earth 's critical zone. *Scientific Reports*, 9(1). https://doi.org/10.1038/s41598-019-40819-9

Holbrook, W. S., Riebe, C. S., Elwaseif, M., Hayes, J. L., Harry, D. L., Basler-Reeder, K., et al. (2014). Geophysical constraints on deep weathering and water storage potential in the Southern Sierra Critical Zone Observatory. *Earth Surface Processes and Landforms*, 39, 366–380. https://doi.org/10.1002/esp.3502

Huang, M. H., Hudson-Rasmussen, B., Burdick, S., Lekic, V., Nelson, M. D., Fauria, K. E., & Schmerr, N. (2021). Bayesian seismic refraction inversion for critical zone science and near-surface applications. *Geochemistry, Geophysics, Geosystems*, 22, e2020GC009172. https://doi. org/10.1029/2020GC009172

Hu, Y., Han, L. G., Liu, Y. S., & Jin, Z. Y. (2020). Wave equation-based local traveltime inversion. *Earth and Space Science*, 7, e2020EA001193. https://doi. org/10.1029/2020EA001193

Klos, P. Z., Goulden, M. L., Riebe, C. S., Tague, C. L., O'Geen, A. T., Flinchum, B. A., et al. (2018). Subsurface plant-accessible water in mountain ecosystems with a Mediterranean climate. *Wiley Interdisciplinary Reviews*: Water. https://doi.org/10.1002/wat2.1277

Köhn, D., Wilken, D., De Nil, D., Wunderlich, T., Rabbel, W., Werther, L., Schmidt, J., Zielhofer, C., & Linzen, S. (2019). Comparison of time-domain SH waveform inversion strategies based on sequential low and bandpass filtered data for improved resolution in near-surface prospecting. *Journal of Applied Geophysics*, *160*, 69–83. https://doi.org/10.1016/j.jappgeo.2018.11.001

Komatitsch, D., & Tromp, J. (1999). Introduction to the spectral element method for three-dimensional seismic wave propagation. *Geophysical Journal International*, *139*(3), 806–822. https://doi.org/10.1046/j.1365-246x.1999.00967.x

Komatitsch, D., Vilotte JP. (1998). The spectral element method: An efficient tool to simulate the seismic response of 2D and 3D geological structures. *Bulletin of the Seismological Society of America*. https://doi.org/10.1785/BSSA0880020368

Lei, W., Ruan, Y., Bozdağ, E., Peter, D., Lefebvre, M., Komatitsch, D., Tromp, J., Hill, J., Podhorszki, N., and Pugmire, D. (2020). Global adjoint tomography—model GLAD-M25. *Geophysical Journal International*, 223(1), 1–21. https://doi.org/10.1093/gji/ggaa253\

Leone, J. D., Holbrook, W. S., Riebe, C. S., Chorover, J., Ferré, T. P. A., Carr, B. J., and Callahan, R. P. (2020). Strong slope-aspect control of regolith thickness by bedrock foliation. *Earth Surface Processes and Landforms*, 45(12), 2998–3010. https://doi.org/10.1002/esp.4947

Li, J., Feng, Z., & Schuster, G. (2016). Wave-equation dispersion inversion. *Geophysical Journal International*, *208*(3), 1567–1578. https://doi.org/10.1093/gji/ggw465

Li, J., Hanafy, S., & Schuster, G.(2018). Wave-Equation dispersion inversion of guided P waves in a waveguide of arbitrary geometry. *Journal of Geophysical Research: Solid Earth*, 123, 7760–7774. https://doi.org/10.1029/2018JB016127

Liu, D.C., Nocedal, J. On the limited memory BFGS method for large scale optimization. *Mathematical Programming* 45, 503–528 (1989). https://doi.org/10.1007/BF01589116

Liu, X., Zhu, T., & Hayes, J. (2022). Critical zone structure by elastic full waveform inversion of seismic refractions in a sandstone catchment, central Pennsylvania, USA. *Journal of Geophysical Research*: Solid Earth, 127, e2021JB023321. https://doi. org/10.1029/2021JB023321

Liu, Z., Li, J., Hanafy, S. M., & Schuster, G. (2019). 3D wave-equation dispersion inversion of Rayleigh Waves. *GEOPHYSICS*, *84*(5). https://doi.org/10.1190/geo2018-0543.1

Mao, J., Sheng, J., Hart, M., and Kim, T. (2016). High-resolution model building with multistage full-waveform inversion for narrow-azimuth acquisition data. *The Leading Edge*, 35(12), 1031–1036. https://doi.org/10.1190/tle35121031.1

McCormick EL, Dralle DN, Hahm WJ, Tune AK, Schmidt LM, Chadwick KD, Rempe DM. Widespread woody plant use of water stored in bedrock. *Nature*. 2021 Sep;597(7875):225-229. doi: 10.1038/s41586-021-03761-3.

Meunier, A., Sardini, P., Robinet, J. C., & Pret, D. (2007). The petrography of weathering processes: Facts and outlooks. *Clay Minerals*, 42(4), 415–435. https://doi.org/10.1180/claymin.2007.042.4.01

Modrak, R. T., Borisov, D., Lefebvre, M., & Tromp, J. (2018). Seisflows—flexible waveform inversion software. *Computers & Geosciences*, *115*, 88–95. https://doi.org/10.1016/j.cageo.2018.02.004

Moravec, B. G., White, A. M., Root, R., Sanchez, A., Olshansky, Y., Paras, B. K., et al. (2020). Resolving deep critical zone architecture in complex volcanic terrain. *Journal of Geophysical Research: Earth Surface*, 125, e2019JF005189. https://doi.org/ 10.1029/2019JF005189

Natural Resources Conservation Service (2015). Crow Creek SNOTEL site, United States Department of Agriculture, SNOTEL surveys. Retrieved from http://wcc.sc.egov.usda.gov/nwcc/site?sitenum=1045, Accessed 07/15/2017.

Navarre-Sitchler, A., Brantley, S. L., & Rother, G. (2015). How porosity increases during incipient weathering of crystalline silicate rocks. *Reviews in Mineralogy and Geochemistry*, 80(1), 331–354. https://doi.org/10.2138/rmg.2015.80.10

Novitsky, C. G., Holbrook, W. S., Carr, B. J., Pasquet, S., Okaya, D., & Flinchum, B. A. (2018). Mapping inherited fractures in the critical zone using seismic aniso- tropy from circular

surveys. *Geophysical Research Letters*, 45, 3126–3135. https://doi.org/10.1002/2017GL075976

Pan, Y., Gao, L., & Bohlen, T. (2019). High-resolution characterization of near-surface structures by surface-wave inversions: From dispersion curve to full waveform. *Surveys in Geophysics*, *40*(2), 167–195. https://doi.org/10.1007/s10712-019-09508-0

Parsekian, A. D., K. Singha, B. J. Minsley,W. S. Holbrook, and L. Slater (2015),Multiscale geophysical imaging of thecritical zone, *Rev. Geophys.*,53,1–26,doi:10.1002/2014RG000465.

Pasquet, S., W. S. Holbrook, B. J. Carr, and K. W. W. Sims (2016), Geophysical imaging of shallow degassing in a Yellowstone hydrothermal system, *Geophys. Res. Lett.*, 43, 12,027–12,035, doi:10.1002/2016GL071306.

Peterman, Z. E., & Hedge, C. E. (1968). Chronology of Precambrian events in the Front Range, Colorado. *Canadian Journal of Earth Sciences*, 5(3), 749–756. https://doi.org/10.1139/e68-073

Pratt, R. G. (1999). Seismic waveform inversion in the frequency domain, part 1: Theory and verification in a physical scale model. *GEOPHYSICS*, *64*(3), 888–901. https://doi.org/10.1190/1.1444597

Riebe, C. S., Hahm, W. J., and Brantley, S. L. (2016). Controls on deep critical zone architecture: A historical review and four testable hypotheses. *Earth Surface Processes and Landforms*, 42(1), 128–156. https://doi.org/10.1002/esp.4052

Sak, P. B., Navarre-Sitchler, A. K., Miller, C. E., Daniel, C. C., Gaillardet, J., Buss, H. L., Lebedeva, M. I., and Brantley, S. L. (2010). Controls on rind thickness on basaltic andesite clasts weathering in Guadeloupe. *Chemical Geology*, 276(3–4), 129–143. https://doi.org/10.1016/j.chemgeo.2010.05.002

Schuster G. T. (2017). *Seismic inversion*. Society of Exploration Geophysicists.

Sheng, J., Leeds, A., Buddensiek, M., & Schuster, G. T. (2006). Early arrival waveform tomography on near-surface refraction data. *GEOPHYSICS*, *71*(4). https://doi.org/10.1190/1.2210969

Smith, J. A., Borisov, D., Cudney, H., Miller, R. D., Modrak, R., Moran, M., Peterie, S. L., Sloan, S. D., Tromp, J., & Wang, Y. (2019). Tunnel detection at Yuma Proving Ground, Arizona, USA — part 2: 3D full-waveform inversion experiments. *GEOPHYSICS*, *84*(1). https://doi.org/10.1190/geo2018-0599.1

St. Clair, J., Moon, S., Holbrook, W. S., Perron, J. T., Riebe, C. S., Martel, S. J., et al. (2015). Geophysical imaging reveals topographic stress control of bedrock weathering. *Science* 350, 534–538. doi: 10.1126/science. aab2210

Tape, C., Liu, Q., Maggi, A., & Tromp, J. (2010). Seismic tomography of the Southern California crust based on spectral-element and adjoint methods. *Geophysical Journal International*, *180*(1), 433–462. https://doi.org/10.1111/j.1365-246x.2009.04429.x

Thurin, J., Brossier, R., & Métivier, L. (2019). Ensemble-based uncertainty estimation in full waveform inversion. *Geophysical Journal International*. https://doi.org/10.1093/gji/ggz384

Toyokuni, G., & Zhao, D. (2021). P-wave tomography for 3-D radial and azimuthal anisotropy beneath Greenland and surrounding regions. *Earth and Space Science*, 8, e2021EA001800. https://doi. org/10.1029/2021EA001800

Tromp, J., & Bachmann, E. (2019). Source encoding for adjoint tomography. *Geophysical Journal International*, *218*(3), 2019–2044. https://doi.org/10.1093/gji/ggz271

Tromp, J., Tape, C., & Liu, Q. (2005). Seismic tomography, adjoint methods, time reversal and banana-doughnut kernels. *Geophysical Journal International*, *160*(1), 195–216. https://doi.org/10.1111/j.1365-246x.2004.02453.x

Wang, W., Chen, P., Keifer, I., Dueker, K., Lee, E.-J., Mu, D., Jiao, J., Zhang, Y., & Carr, B. (2019 a). Weathering Front under a granite ridge revealed through full-3d seismic ambient-noise tomography. *Earth and Planetary Science Letters*, *509*, 66–77. https://doi.org/10.1016/j.epsl.2018.12.038

Wang, W., Chen, P., Lee, E.-J., and Mu, D. (2019 b). Full-3D Seismic Tomography for Structure of the Critical Zone. *In Earthquake and Disaster Risk: Decade Retrospective of the Wenchuan Earthquake* (pp. 203–231). essay, Higher Education Press and Springer Nature Singapore .

Wang, Y., Miller, R. D., Peterie, S. L., Sloan, S. D., Moran, M. L., Cudney, H. H., Smith, J. A., Borisov, D., Modrak, R., & Tromp, J. (2019 c). Tunnel detection at Yuma Proving Ground, Arizona, USA — part 1: 2D full-waveform inversion experiment. *GEOPHYSICS*, *84*(1). https://doi.org/10.1190/geo2018-0598.1

West, N., Kirby, E., Nyblade, A. A., and Brantley, S. L. (2019). Climate preconditions the critical zone: Elucidating the role of subsurface fractures in the evolution of asymmetric topography. *Earth and Planetary Science Letters*, 513, 197–205. https://doi.org/10.1016/j.epsl.2019.01.039

Virieux, J., & Operto, S. (2009). An overview of full-waveform inversion in exploration geophysics. *GEOPHYSICS*, 74(6). https://doi.org/10.1190/1.3238367

Xia, J., Miller, R. D., & Park, C. B. (1999). Estimation of near-surface shear-wave velocity by inversion of Rayleigh Waves. *GEOPHYSICS*, *64*(3), 691–700. https://doi.org/10.1190/1.1444578

Yuan, Y. O., Simons, F. J., & Bozdağ, E. (2015). Multiscale adjoint waveform tomography for surface and body waves. *GEOPHYSICS*, 80(5). https://doi.org/10.1190/geo2014-0461.1

Yuan, Y. O., Simons, F. J., and Tromp, J. (2016). Double-difference adjoint seismic tomography. *Geophysical Journal International*, *206*(3), 1599–1618. https://doi.org/10.1093/gji/ggw233

Zielinski, R. A., Peterman, Z. E., Stuckless, J. S., Rosholt, J. N., & Nkomo, I. T. (1982). The chemical and isotopic record of rock-water interaction in the Sherman granite, Wyoming and Colorado. *Contributions to Mineralogy and Petrology*, 78(3), 209–219. https://doi.org/10.1007/BF00398915